Tunneling and Thermally-Activated Electron Transfer in Dye-Sensitized $SnO_2|TiO_2$ Core|Shell Nanostructures

Journal:	*Journal of the American Chemical Society*
Manuscript ID	ja-2020-09349c
Manuscript Type:	Article
Date Submitted by the Author:	31-Aug-2020
Complete List of Authors:	Bangle, Rachel; University of North Carolina at Chapel Hill, Chemistry Mortelliti, Michael; University of North Carolina at Chapel Hill, Chemistry Troian-Gautier, Ludovic; University of North Carolina at Chapel Hill, Chemistry; Université Libre de Bruxelles, Laboratoire de Chimie Organique Dempsey, Jillian; University of North Carolina at Chapel Hill, Chemistry Meyer, Gerald; University of North Carolina at Chapel Hill, Department of Chemistry

Tunneling and Thermally-Activated Electron Transfer in Dye-Sensitized $SnO_2|TiO_2$ Core|Shell Nanostructures

Rachel E. Bangle,[†] Michael J. Mortelliti,[†] Ludovic Troian-Gautier,[†§] Jillian L. Dempsey,[†]* and Gerald J. Meyer[†]*

[†] Department of Chemistry, University of North Carolina at Chapel Hill, Chapel Hill, North Carolina, 27599-3290, United States.

[§] Present address: Laboratoire de Chimie Organique, Université libre de Bruxelles (ULB), CP 160/06, 50 avenue F.D. Roosevelt, 1050 Brussels, Belgium.

* To whom correspondence should be addressed: gjmeyer@email.unc.edu, dempseyj@email.unc.edu

Abstract

The mechanism for interfacial electron transfer (ET) from a metal oxide core|shell nanostructure to a $[Ru^{III}(2,2'\text{-bipyridine})_2(4,4'\text{-}(PO_3H_2)_2 2,2'\text{-bipyridine})]^{3+}$ sensitizer was probed through spectroscopic quantification of the ET kinetics over a 70 °C temperature range in aqueous 0.1 M $HClO_4$ solution. Mesoporous thin films of rutile SnO_2 or insulating ZrO_2 nanocrystals were coated through atomic layer deposition with TiO_2 shells of variable thickness to comprise the core|shell nanostructures. In agreement with previous research, Raman spectroscopy and transmission electron microscopy provided evidence that annealing the mesoporous $SnO_2|TiO_2$ materials at 450 °C resulted in rutile TiO_2 shells. Materials heated to only 200 °C, termed 'unannealed,' exhibited no evidence of crystallinity. Annealed and unannealed materials resulted in dissimilar interfacial ET kinetics. While temperature-independent kinetics indicated ET occurred through tunneling in the thickest unannealed shells, materials with annealed shells underwent thermally-activated ET. Further, thermally-activated ET and tunneling competed in materials with unannealed shells less than 50 ALD-cycles thick. Arrhenius analysis of the thermally-activated ET revealed large barriers, consistent with slow ET reactions for $SnO_2|TiO_2$ relative to SnO_2 or TiO_2 alone. Barriers were factors of three to four larger for unannealed $SnO_2|TiO_2$ materials than those observed upon annealing. Eyring analysis revealed that Gibbs free energies of activation were largely insensitive to heat treatment, $\Delta G^{\ddagger} = 47 \pm 3$ kJ/mol, and were entropically favored for unannealed $SnO_2|TiO_2$ and entropically costly for annealed. A model is proposed wherein ET in annealed $SnO_2|TiO_2$ is rate limited by electron transport in the shell, while ET in unannealed $SnO_2|TiO_2$ is rate limited by electron escape from the core. The model is consistent with a comparative study of $ZrO_2|TiO_2$ materials for which insulating ZrO_2 cores are energetically inaccessible to electrons. These mechanistic insights provide guidance on how to manipulate core|shell nanostructures for applications in solar water splitting.

Introduction

Metal oxide nanostructures, which are composed of a core of one metal oxide and a shell of another, are promising materials for applications in sensitized photoelectrodes,[1–3] gas sensors,[4] batteries,[5,6] and perovskite solar cells.[7] A particularly promising core|shell material for solar energy conversion applications is a SnO_2 core with a TiO_2 shell generated by atomic layer deposition (ALD), abbreviated $SnO_2|TiO_2$.[8–13] In regenerative dye-sensitized solar cells, mesoporous thin films of $SnO_2|TiO_2$ have higher efficiencies than do films of SnO_2 alone.[8,11,13] For dye-sensitized water oxidation, the $SnO_2|TiO_2$ materials are superior to either TiO_2 or SnO_2.[9,10] The improved performance is generally attributed to inhibited recombination of the injected electrons ($MO_2(e^-)$) with the oxidized sensitizer or catalyst (S^+), Eq. 1.

$$MO_2(e^-)|\text{-}S^+ \rightarrow MO_2|\text{-}S \quad (1)$$

The origins of the slowed charge recombination, however, remain uncertain.[1,12,14–17] Previous researchers have proposed a band edge offset model to rationalize the slow interfacial electron transfer (ET) in $SnO_2|TiO_2$, referring to the disparate band edge minima of the two oxides— the conduction band edge minimum of rutile SnO_2 is ~ 0.5 eV more positive than that of rutile TiO_2. Hence, in this model, an electron in the SnO_2 core must move through or over a 0.5 eV barrier to undergo ET to molecular acceptors.[15] Because of the difficulty of overcoming such a large barrier, ET has been proposed by several researchers to occur through tunneling, an assignment generally supported by an exponential dependence of the ET rate constant on the shell thicknesses.[12,14–17] Importantly, all of these studies, and the few which invoke a thermally activated mechanism,[12,14,16] were performed at a single temperature, so the mechanistic assignments remain speculative. Further, the band edge offset model relies on band edge positions of crystalline materials measured in aqueous solution and ignores the large spread (~ 1 V) of reported flat band potentials[18–20] as well as the possibility of a mixed oxide phase at the $SnO_2|TiO_2$ interface.[21–23]

Here we quantify the electron transfer described in Eq. 1 over a 70 °C temperature range for mesoporous thin films of rutile SnO_2, rutile TiO_2, anatase TiO_2, $ZrO_2|TiO_2$, and $SnO_2|TiO_2$ sensitized to visible light with [Ru(2,2′-bipyridine)$_2$(4,4′-bis(phosphonic acid)-2,2′-bipyridine)]$^{2+}$ (RuP) which is thermally competent to drive water oxidation. The temperature dependent kinetic studies reported here enable direct assignment of the underlying electron transfer mechanism(s) as activated or tunneling. Comparative studies with rutile SnO_2 and both the anatase and rutile polymorphs of TiO_2 show an ~ six-fold smaller barrier for ET from SnO_2, which undoubtedly underlies the reported efficiency improvements of TiO_2-based dye-sensitized solar cells.[24,25] In sensitized $SnO_2|TiO_2$, Arrhenius and Eyring analysis as a function of shell thickness and post-deposition heat treatment provide the detailed mechanistic insights necessary to propose a predictive model for interfacial ET. This model is supported by temperature-dependent kinetics observed in sensitized $ZrO_2|TiO_2$, where the insulator ZrO_2 precludes electron transport to the core.

Results

Characterization of $SnO_2|TiO_2$ Core|Shell Films

Mesoporous thin films of rutile SnO_2 nanocrystals, which are quasi-spherical and ~ 10 nm in diameter, form mesoporous films that have been characterized previously.[26] Atomic layer deposition (ALD) of TDMA-Ti onto this SnO_2 enabled fabrication of $SnO_2|XTiO_2$ core|shell materials, where X is the number of ALD cycles. After TiO_2 deposition, $SnO_2|XTiO_2$ materials termed 'unannealed' were heated to 200 °C for 30 minutes, while $SnO_2|XTiO_2$ termed 'annealed' were heated to 450 °C. As shown in HRTEM images (Figs. 1, S1, S2), deposition of 10 cycles of TiO_2 results in films nearly indistinguishable from bare SnO_2, while deposition of 20, 30, or 50 cycles of TiO_2 results in smooth shells that progressively thicken with X. As observed previously, application of 50 ALD cycles of TiO_2 partially fills the mesoporous void spaces in the SnO_2.[14,21,26,31–33] In both annealed and unannealed materials, rutile SnO_2 cores are identifiable in HRTEM images (Fig 1) by lattice fringes with 0.330 nm and 0.260 nm d-space value, which are characteristic of the SnO_2 (110) and (101) crystalline planes, respectively. Unannealed TiO_2 shells exhibit no discernable lattice fringes (Fig 1a-d), while annealed TiO_2 shells exhibit lattice fringes with 0.320 nm, 0.250 nm, 0.220 nm, and/or 0.170 nm d-space values. The TiO_2 matrix for $SnO_2|50TiO_2$, which partially fills the SnO_2 pores, was highly polycrystalline, which increased the uncertainty of d-space measurements, with standard deviations from ±0.010 nm to ±0.017 nm. Nevertheless, these lattice spacings in the annealed materials are characteristic of rutile TiO_2 (*r*-TiO_2) (110), (101), (111), and (211) crystalline planes, respectively (Fig 1e-h).

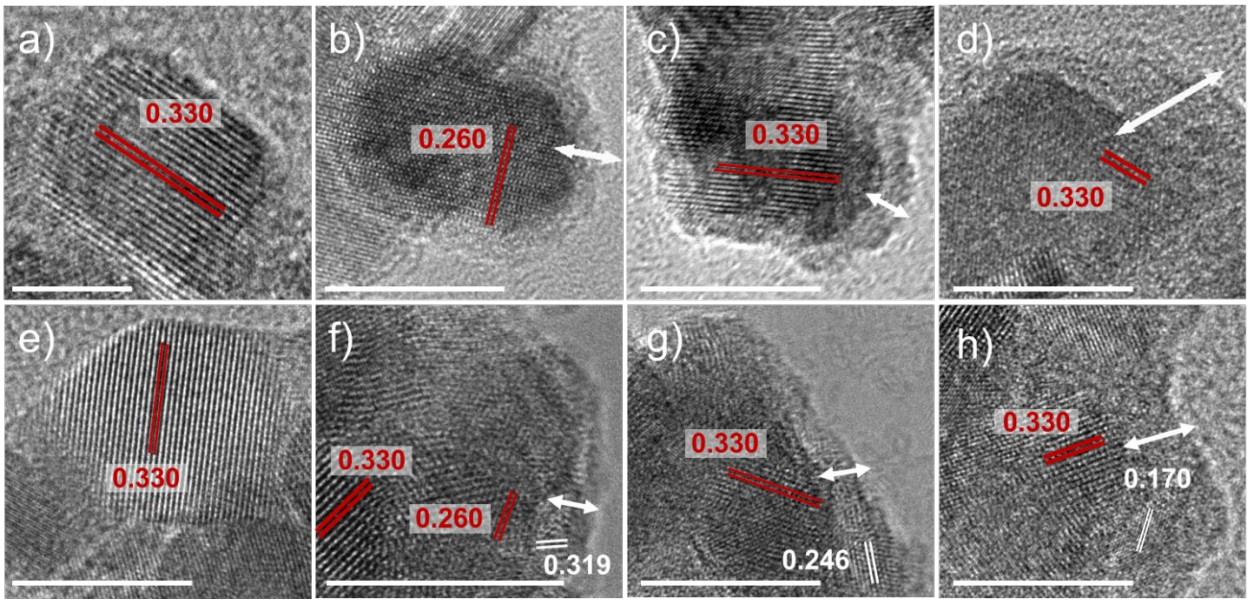

Figure 1. HRTEM images of unannealed a) $SnO_2|10TiO_2$, b) $SnO_2|20TiO_2$, c) $SnO_2|30TiO_2$, and d) $SnO_2|50TiO_2$ and annealed e) $SnO_2|10TiO_2$, f) $SnO_2|20TiO_2$, g) $SnO_2|30TiO_2$, and h) $SnO_2|50TiO_2$. White bars at the bottom of each image represent a 10 nm scale. Annealed materials were treated at 450 °C after ALD, while unannealed materials were treated at 200 °C. Each ALD cycle indicated as X in $SnO_2|XTiO_2$ is estimated to deposit ~ 0.66 Å TiO_2. White arrows denote the TiO_2 shells, red lines represent the lattice fringe measurements characteristic of SnO_2, and white lines represent the lattice fringe measurements characteristic of *r*-TiO_2. These magnified images are portions of Figs. S1 and S2.

Annealed and unannealed $SnO_2|XTiO_2$ materials also exhibit distinctive Raman spectra (Fig. 2). Rutile SnO_2 displays prominent E_g and A_{1g} phonon modes at 476 and 633 cm^{-1} respectively, a broad band centered at 560 cm^{-1} (labeled S_1) ascribed to a non-stoichiometric SnO_x species, and small features at 245 and 310 cm^{-1} attributable to infrared-active phonon modes with E_u symmetry.[26,34–40] In unannealed $SnO_2|XTiO_2$ materials, addition of TiO_2 layers progressively depresses the S_1 band, enhances the A_{1g} and E_u modes, and generally broadens features, but no clear new bands arise. In contrast, addition of annealed TiO_2 results in progressive growth of a small spectral feature at 245 cm^{-1} and broad peaks centered at 430 and 603 cm^{-1}. These peaks are not visible in $SnO_2|10TiO_2$ and are unclear in $SnO_2|20TiO_2$, but are easily distinguished in annealed $SnO_2|30TiO_2$ and $SnO_2|50TiO_2$. The peak positions are consistent with the reported Raman spectrum of *r*-TiO_2 multi-phonon, A_{1g}, and E_g modes, respectively.[41,42]

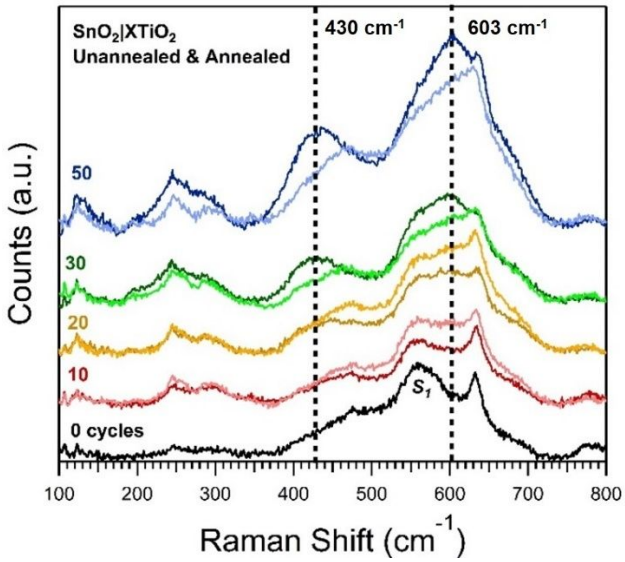

Figure 2. Raman spectra of unannealed (light) and annealed (dark) $SnO_2|XTiO_2$ where X is the number of cycles of TiO_2 deposited, indicated on the left. Each ALD cycle is estimated to deposit ~ 0.66 Å TiO_2.

Previous reports have established that ALD-generated TiO_2 coatings are amorphous when deposited at temperatures below 150-250° C, while exposure to higher temperatures leads to either anatase TiO_2 (*a*-TiO_2,150-400 °C) or *r*-TiO_2 (> 300 °C).[43–45] Growth of *r*-TiO_2 has been reported at lower temperatures, however, on SnO_2 and other rutile substrates.[46,47] This literature precedence is in line with HRTEM and Raman evidence for *r*-TiO_2 in annealed shells, heated to 450 °C, and the lack of evidence for crystalline TiO_2 in unannealed shells, heated to 200 °C. In total HRTEM images, Raman spectra, and previous literature are consistent with the assignment of TiO_2 shells in 'annealed' $SnO_2|XTiO_2$ as rutile and in 'unannealed' $SnO_2|XTiO_2$ as amorphous.

Characterization of $ZrO_2|TiO_2$ Core|Shell Films

Nanocrystals of ZrO_2 form mesoporous films analogous to the SnO_2 materials. Analysis of this ZrO_2 by HRTEM reveals quasi-spherical nanocrystals with an average size of 14 ± 6 nm. A

small population of larger nanocrystals possess a more rod-like morphology (Fig. S3). Atomic layer deposition of TiO_2 onto ZrO_2 nanocrystalline films results in $ZrO_2|XTiO_2$ materials, which are heat treated for 30 minutes at either 200 °C (unannealed) or 450 °C (annealed). As for $SnO_2|10TiO_2$, HRTEM images of unannealed and annealed $ZrO_2|10TiO_2$ are nearly indistinguishable from ZrO_2 alone (Figs. S4-S5). A smooth shell without discernable lattice fringes is observed for 20, 30, and 50 unannealed TiO_2 cycles (Fig. S4). Annealed $ZrO_2|XTiO_2$ samples with at least 20 ALD cycles of TiO_2 have visible shells that appear to have continuous lattice fringes extending to the edges of the nanocrystals (Fig. S5).

Raman spectra of ZrO_2 materials (Fig. S6) display peaks indicative of monoclinic and tetragonal ZrO_2 phases, assignments supported by the observed x-ray diffraction pattern (Fig. S7).[48] Deposition of 10 ALD cycles of TiO_2 results in Raman spectra nearly indistinguishable from that of ZrO_2, regardless of post-deposition heat treatment. Raman spectra of unannealed $ZrO_2|20TiO_2$ and $ZrO_2|30TiO_2$ weakly exhibit additional peaks at 150 and 421 cm^{-1} which become prominent in unannealed $ZrO_2|50TiO_2$ (Fig. S6a). Occurrence of these features is accompanied by a shift of ZrO_2 x-ray diffraction peaks to larger 2θ values (Fig. S7). Upon annealing, the Raman peaks at 150 and 421 cm^{-1} are enhanced and an additional peak at 531 cm^{-1} arises for $ZrO_2|30TiO_2$ and $ZrO_2|50TiO_2$ (Fig. S6). The sharp peak at 150 cm^{-1} is consistent with the E_g phonon mode of anatase TiO_2 (*a*-TiO_2), while the peaks at 421 cm^{-1} and 531 cm^{-1} most closely resemble prominent modes of $ZrTiO_4$.[42,49–54]

Raman and HRTEM evidence thus suggest that shells in annealed $ZrO_2|XTiO_2$ consist of *a*-TiO_2 with $ZrTiO_4$ species at the interface. For unannealed $ZrO_2|XTiO_2$, despite lack of evidence for crystallinity in HRTEM, Raman spectra indicate that some portions of the thickest TiO_2 shells are anatase. However, interposition of thin ALD layers of amorphous Al_2O_3 between the SnO_2 and unannealed TiO_2 shells, as described in SI, removes the 150 and 421 cm^{-1} Raman peaks, suggesting shells in these materials remain amorphous. Annealing these $SnO_2|Al_2O_3|TiO_2$ materials returns the sharp Raman peak indicative of *a*-TiO_2 at 150 cm^{-1}, but no features characteristic of $ZrTiO_4$ (Fig. S8).[49–54]

Sensitization with RuP

Mesoporous, nanocrystalline thin films of SnO_2 and ZrO_2 are nearly transparent to visible light (Fig. 3a and Fig. S9a). Addition of ALD TiO_2 generates progressively more opaque films that both scatter more light and exhibit lower energy fundamental absorbance features, consistent with previous literature.[21] Films were sensitized to visible light with surface-anchored RuP, as indicated by the characteristic RuP metal-to-ligand charge transfer (MLCT) absorption peak (Fig. 3b and Fig. S9b). Surface coverages of RuP, Γ, were calculated from the MLCT absorbance using Eq. 2 (Table 1), where A_{max} is the maximum MLCT absorption, and ε_{max} is the molar absorption coefficient of RuP at the same wavelength (13,300 M^{-1} cm^{-1}, 460 nm).[55]

$$\Gamma = \frac{A_{max}}{1000 \times \varepsilon_{max}} \quad (2)$$

Deposition of TiO_2 lowers the attainable Γ as pore filling results in smaller available surface areas. Additionally, Γ values are generally larger for unannealed over annealed core|shell materials and for $ZrO_2|TiO_2$ over $SnO_2|TiO_2$.

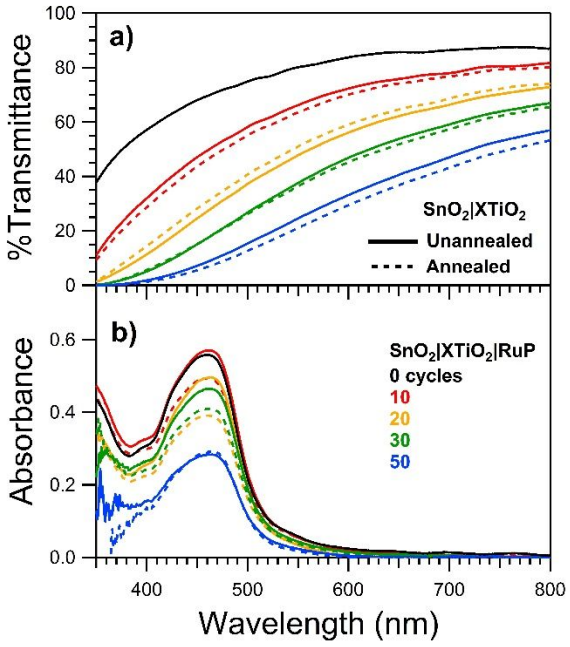

Figure 3. UV-Visible spectra acquired in aqueous 0.1 M $HClO_4$ for a) unsensitized and b) RuP-sensitized $SnO_2|XTiO_2$ materials, where X is the number of ALD cycles. Each ALD cycle is estimated to deposit ~ 0.66 Å TiO_2. Solid lines represent unannealed films, while dashed lines represent annealed. Spectra in b) were generated by subtraction of the spectra of the unsensitized materials from spectra of RuP-sensitized films.

.

Table 1. RuP Surface Coverage, Γ, in Sensitized Core|Shell Materials

	Γ (x 10^{-8} mol cm^{-2})			
	$SnO_2|XTiO_2$		**$ZrO_2|XTiO_2$**	
X	**Annealed**	**Unannealed**	**Annealed**	**Unannealed**
10	3.7	4.3	4.1	4.5
20	2.9	3.7	4.2	4.5
30	3.1	3.5	4.3	5.2
50	2.2	2.1	2.3	2.4

Temperature Dependence of Interfacial Electron Transfer

Transient absorption spectroscopy in N_2-sparged aqueous 0.1 M $HClO_4$ solution was employed to quantify interfacial electron transfer (ET) pseudo-rate constants for annealed and unannealed $SnO_2|XTiO_2$. As shown in Scheme 1, pulsed 532 nm light generates a RuP excited

state which rapidly transfers an electron into poorly-defined acceptor states in the core|shell material. Within the 10 ns instrument response time, this forms an oxidized RuP molecule—signified by a long-lived decrease in the RuP MLCT absorbance (ΔA) spanning ~ 385–500 nm—and an excess electron in the $SnO_2|TiO_2$. The core|shell electron then recombines through interfacial ET with the oxidized sensitizer (Eq. 1, Scheme 1), and the RuP transient spectral change returns to the initial absorbance. The ET was monitored at 402 nm, which is an isosbestic point of the RuP excited state transient absorption spectrum, as a function of temperature from 10 to 80 °C for both annealed and unannealed RuP-sensitized $SnO_2|TiO_2$ materials with shells of variable thicknesses (Fig. 4, Figs. S10-S11). In all cases, initial absorption magnitudes are recovered within 5 ms, indicating no net photochemistry occurs. Small sample-to-sample adjustments to the laser fluence ensured nearly constant initial ΔA.[56] For the majority of $SnO_2|XTiO_2$ variations, ET accelerates at high temperatures, with the exception of unannealed $SnO_2|50TiO_2$ for which ET kinetics are temperature independent.

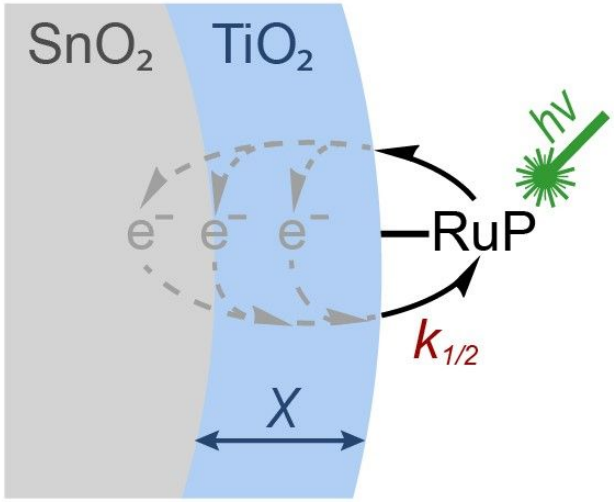

Scheme 1. A SnO_2 nanoparticle core is coated with a TiO_2 shell through ALD. The number of applied ALD cycles (X) controls the shell thickness. Materials are sensitized with RuP, which is excited with pulsed 532 nm light to initiate electron transfer from the RuP excited state into the material. The acceptor states in the core/shell are poorly defined and could exist in the core, shell, or interface (gray arrows). Electrons in the material then recombine with the photo-oxidized RuP through interfacial ET with rate constant $k_{1/2}$, as reflected in the observed transient spectral changes.

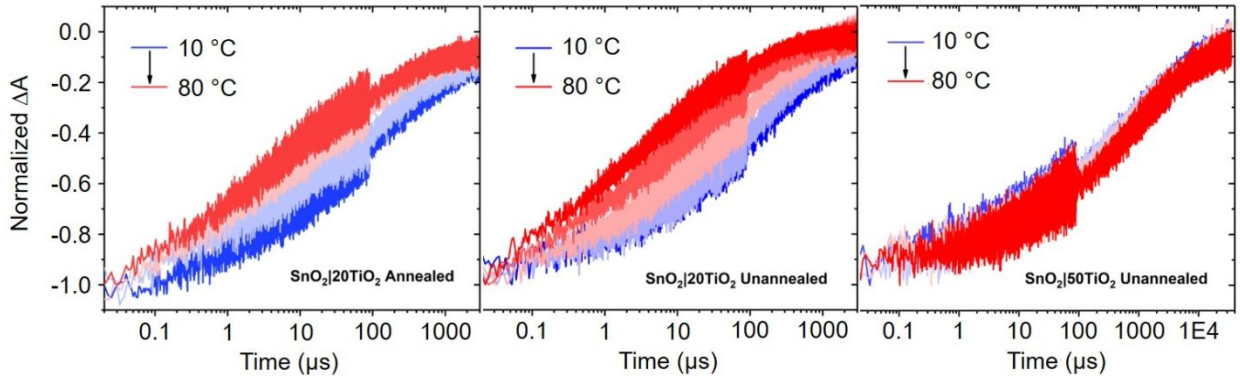

Figure 4. Transient absorption changes (ΔA) monitored in aqueous 0.1 M $HClO_4$ at 402 nm over the indicated temperature ranges following pulsed 532 nm light excitation of RuP-sensitized $SnO_2|XTiO_2$ films, where X is the number of ALD TiO_2 cycles. Each ALD cycle is estimated to deposit ~ 0.66 Å TiO_2. Shells were either annealed (heated to 450 °C) or unannealed (heated to 200 °C) post deposition as indicated.

As frequently reported in mesoporous metal oxide materials, interfacial ET kinetics were non-exponential.[57,58] As such, interfacial ET pseudo-rate constants, $k_{1/2}$, were approximated as the inverse of the time required for ΔA at 20 ns to decay by half. Arrhenius plots (Fig. 5) show that core|shell materials annealed at 450 °C post TiO_2 deposition manifest exclusively linear temperature dependence of $\ln(k_{1/2})$ values from 10 to 80 °C. In contrast, unannealed $SnO_2|10TiO_2$, $SnO|20TiO_2$, and $SnO_2|30TiO_2$, each heated to 200 °C post TiO_2 deposition, exhibit non-linear Arrhenius plots. Values of $\ln(k_{1/2})$ are nearly temperature-independent below ~ 40 °C, but increase linearly (and remarkably steeply for $SnO_2|20TiO_2$ and $SnO_2|30TiO_2$) at higher temperatures. Temperature-independent ET is observed across the entire probed range for unannealed $SnO_2|50TiO_2$.

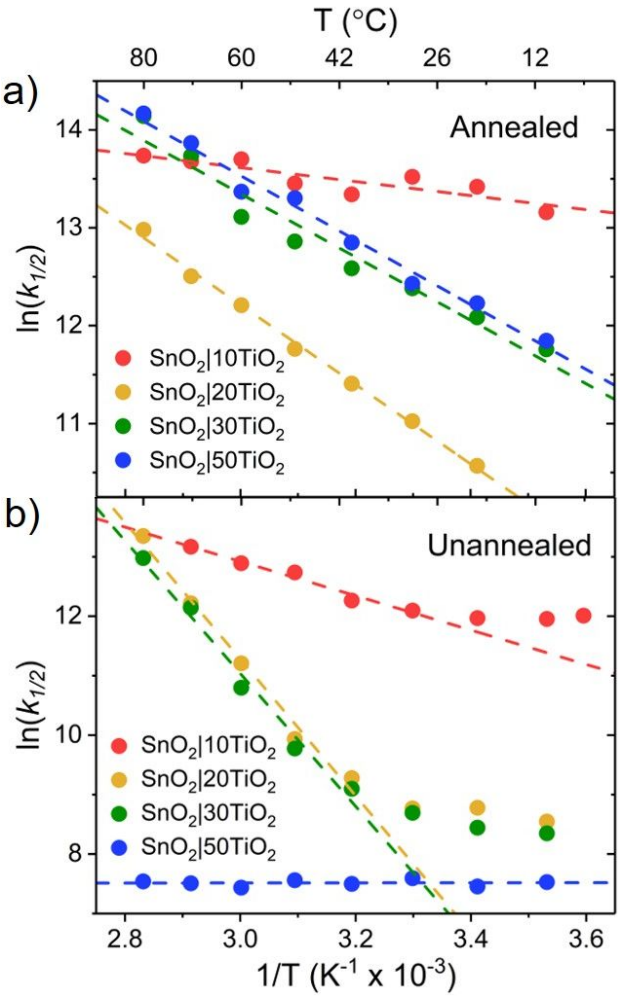

Figure 5. Arrhenius analysis of interfacial electron transfer following 532 nm pulsed light excitation in aqueous 0.1 M $HClO_4$ for RuP-sensitized $SnO_2|XTiO_2$ films, where X in the number of ALD TiO_2 cycles. Each ALD cycle is estimated to deposit ~ 0.66 Å TiO_2. Materials were heated post TiO_2 deposition for 30 min to either a) 450 °C (annealed) or b) 200 °C (unannealed). Dashed lines represent fits of the linear portions of the data to Eq. 3.

Analogous reference studies were performed for RuP-sensitized rutile SnO_2, *r*-TiO_2, and *a*-TiO_2 mesoporous thin films. Transient spectral changes for SnO_2 and *a*-TiO_2 were measured at 402 nm after 532 nm pulsed light excitation as a function of temperature (Fig. S12). The fundamental absorbance of *r*-TiO_2 prevented spectroscopic detection at 402 nm, so spectral changes were instead monitored at 460 nm. Pseudo-rate constants of ET for both *r*-TiO_2 and *a*-TiO_2 increase with temperature to a similar degree, while for SnO_2, ET pseudo-rate constants increase only slightly with temperature (Fig. 6).

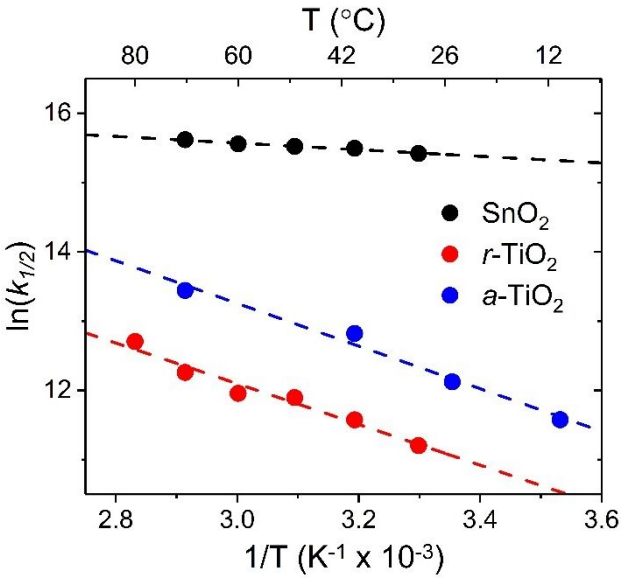

Figure 6. Arrhenius analysis of interfacial electron transfer following 532 nm pulsed light excitation in aqueous 0.1 M $HClO_4$ for RuP-sensitized SnO_2, rutile TiO_2 (*r*-TiO_2), and anatase TiO_2 (*a*-TiO_2). Dashed lines represent fits to Eq. 3.

Interfacial ET pseudo rate constants were also quantified as a function of temperature from transient spectral changes for RuP-sensitized ZrO_2|XTiO_2 materials (Figs. S13-S14). Insulating ZrO_2 cores possess high-energy acceptor states which are thought to be inaccessible to the RuP excited state, forcing injected electrons to reside exclusively in the TiO_2 shell.[14,17] Here, the kinetic response to temperature was insensitive to the post-deposition heat treatment (Fig. 7). For annealed and unannealed ZrO_2|10TiO_2, $k_{1/2}$ increases only slightly with temperature. For all other ZrO_2|XTiO_2 materials, Arrhenius plots display similar slopes, greater than that of ZrO_2|10TiO_2. Kinetics were within error the same when a thin layer of amorphous Al_2O_3 was deposited onto the ZrO_2 prior to TiO_2 deposition to form unannealed ZrO_2|Al_2O_3|50TiO_2 (Fig. S15).[59]

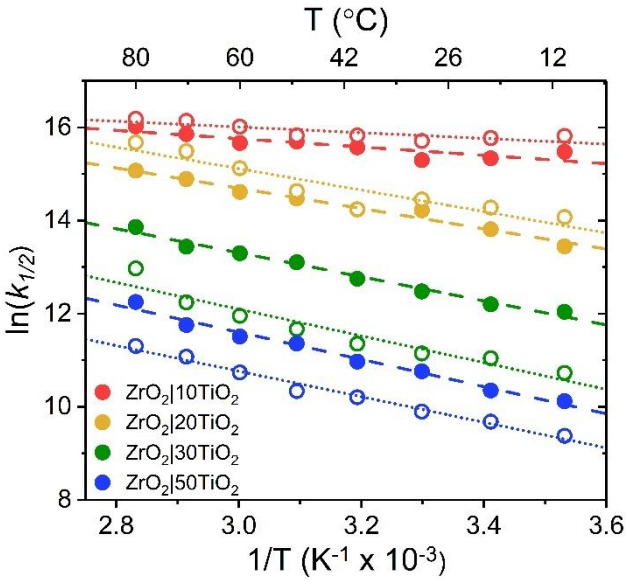

Figure 7. Arrhenius plots of interfacial electron transfer following 532 nm pulsed light excitation in aqueous 0.1 M $HClO_4$ for RuP-sensitized $ZrO_2|XTiO_2$ films, where X in the number of ALD TiO_2 cycles, that were either annealed (solid circles, dashed lines) or unannealed (open circle, dotted lines) post TiO_2 deposition. Each ALD cycle is estimated to deposit ~ 0.66 Å TiO_2. Dashed lines represent fits to Eq. 3.

Arrhenius and Eyring Analyses

The Arrhenius equation states that thermally-activated electron transfer rate constants are defined by a pre-exponential frequency factor A, the temperature T, and an activation energy E_a (Eq. 3).

$$\ln k_{1/2} = \left(\frac{E_a}{R}\right)\frac{1}{T} + \ln A \qquad (3)$$

Under conditions in which interfacial ET rate constants depend exponentially on temperature, E_a vales were quantified from Arrhenius plots (Fig. 5-7) using Eq. 3 (Table 2, Fig. 8). For SnO_2, E_a is small— ~ 4 kJ mol^{-1}, and *a*- and *r*-TiO_2 display equal E_a values— ~ 24 kJ mol^{-1}. In annealed $SnO_2|TiO_2$ films, E_a is ~ 6 kJ mol^{-1} for $SnO_2|10TiO_2$, but ~ 30 kJ mol^{-1} for materials with thicker shells.[60] The same is true for both annealed and unannealed $ZrO_2|XTiO_2$. In unannealed $SnO_2|XTiO_2$, significantly larger E_a values are observed— ~ 25 kJ mol^{-1} for $SnO_2|10TiO_2$ and ~ 95 kJ mol^{-1} for $SnO_2|20TiO_2$ and $SnO_2|30TiO_2$.

Table 2. Activation Energies, E_a, for Interfacial Electron Transfer

	E_a (kJ mol^{-1})	
	Annealed [a]	**Unannealed** [b]
SnO_2	4 ± 1	
***r*-TiO_2**	24 ± 4	

***a*-TiO_2**	24 ± 2	
SnO_2|10TiO_2	6 ± 3	25 ± 3
SnO_2|20TiO_2	34 ± 4	96 ± 10
SnO_2|30TiO_2	27 ± 3	93 ± 11
SnO_2|50TiO_2	27 ± 3	-
ZrO_2|10TiO_2	7 ± 2	5 ± 1
ZrO_2|20TiO_2	18 ± 1	19 ± 5
ZrO_2|30TiO_2	22 ± 3	24 ± 2
ZrO_2|50TiO_2	24 ± 1	23 ± 3

[a] Heated to 450 °C for 30 min in air after TiO_2 deposition.
[b] Heated to 200 °C for 30 min in air after TiO_2 deposition.

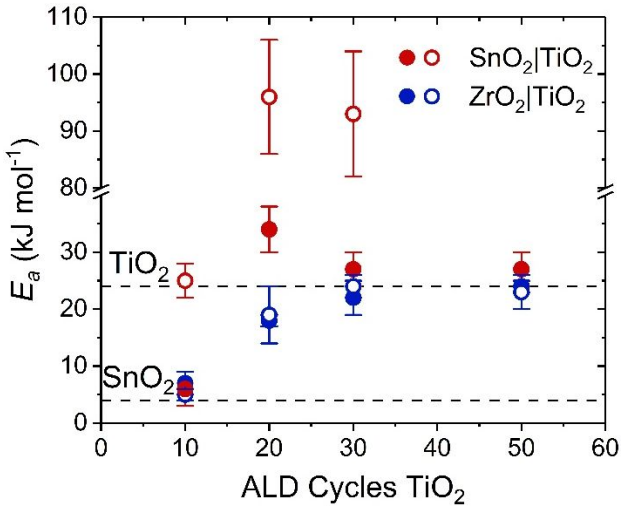

Figure 8. Activation energies, E_a, for temperature-dependent interfacial electron transfer on core|shell films in aqueous 0.1 M $HClO_4$ as a function of shell thickness, represented by the number of ALD cycles of TiO_2. Each ALD cycle is estimated to deposit ~ 0.66 Å TiO_2. Annealed shells are represented as solid circles, while unannealed shells are represented as open circles. SnO_2|TiO_2 films are shown in red, and ZrO_2|TiO_2 films are shown in blue. Reference E_a values for SnO_2 and TiO_2 are shown as dashed lines. Equal values of E_a were obtained for *a*-TiO_2 and *r*-TiO_2.

Similarly, the Eyring equation, Eq. 4, describes thermally-activated ET rate constants in terms of the enthalpy, $\Delta H^{\ddagger}$, and entropy, $\Delta S^{\ddagger}$, of activation, which allow calculation of the Gibbs free energy of activation, $\Delta G^{\ddagger}$ (Table 3, Fig. S16).

$$\ln\left(\frac{k}{T}\right) = \frac{-\Delta H^{\ddagger}}{R}\frac{1}{T} + \ln\left(\frac{k_b}{h}\right) + \frac{\Delta S^{\ddagger}}{R} \qquad (4)$$

It should be noted that $\Delta S^{\ddagger}$ and $\Delta G^{\ddagger}$ depend on the absolute values of the ET rate constants, while in this study $k_{1/2}$ pseudo-rate constants serve as proxies. As such, the internal comparisons of $\Delta S^{\ddagger}$ and $\Delta G^{\ddagger}$ are more meaningful than absolute values.

Table 3. Enthalpies, $\Delta H^{\ddagger}$, Entropies, $\Delta S^{\ddagger}$, and Gibbs Free Energies, $\Delta G^{\ddagger}$, of Activation

	Annealed [a]			Unannealed [b]		
	$\Delta H^{\ddagger}$ (kJ mol^{-1})	$\Delta S^{\ddagger}$ (J mol^{-1} K^{-1})	$\Delta G^{\ddagger}$ [c] (kJ mol^{-1})	$\Delta H^{\ddagger}$ (kJ mol^{-1})	$\Delta S^{\ddagger}$ (J mol^{-1} K^{-1})	$\Delta G^{\ddagger}$ [c] (kJ mol^{-1})
SnO_2|10TiO_2	3 ± 1	-123 ± 3	44 ± 2	21 ± 2	-74 ± 5	46 ± 3
SnO_2|20TiO_2	31 ± 1	-51 ± 2	48 ± 1	93 ± 5	130 ± 15	51 ± 9
SnO_2|30TiO_2	24 ± 2	-62 ± 6	45 ± 4	90 ± 6	120 ± 15	51 ± 10
SnO_2|50TiO_2	25 ± 1	-59 ± 3	44 ± 2	-	-	-
ZrO_2|10TiO_2	10 ± 1	12 ± 4	6 ± 3	8 ± 1	7 ± 4	5 ± 2
ZrO_2|20TiO_2	21 ± 1	35 ± 3	9 ± 2	22 ± 3	44 ± 7	7 ± 5
ZrO_2|30TiO_2	24 ± 1	34 ± 3	13 ± 2	26 ± 2	27 ± 7	18 ± 4
ZrO_2|50TiO_2	27 ± 1	28 ± 3	18 ± 2	25 ± 1	17 ± 3	20 ± 2

[a] Heated to 450 °C after TiO_2 deposition.
[b] Heated to 200 °C after TiO_2 deposition
[c] Calculated as $\Delta G^{\ddagger} = \Delta H^{\ddagger} - T\Delta S^{\ddagger}$ for 60 °C.

Values of $\Delta H^{\ddagger}$ are analogous to E_a values quantified through Arrhenius analysis, and display the same trends with core identity, shell thickness, and post-deposition heat treatment. Values of $\Delta S^{\ddagger}$, however, provide new insights (Fig. 9).[61] For ZrO_2|XTiO_2, values of $\Delta S^{\ddagger}$ are insensitive to post-deposition heat treatment and are near 0 J mol^{-1} K^{-1}. Annealed SnO_2|XTiO_2 and unannealed SnO_2|10TiO_2 undergo ET with large negative $\Delta S^{\ddagger}$, between –50 and –120 J mol^{-1} K^{-1}. In stark contrast, unannealed SnO_2|20TiO_2 and SnO_2|30TiO_2 undergo ET with $\Delta S^{\ddagger} \approx +125$ J mol^{-1} K^{-1}. Values of $\Delta H^{\ddagger}$ and $\Delta S^{\ddagger}$ were used to calculate $\Delta G^{\ddagger}$ at 60 °C (Table 3), a temperature at which ET is temperature dependent in all materials except unannealed SnO_2|50TiO_2. For ZrO_2|XTiO_2, $\Delta G^{\ddagger}$ increased linearly with shell thickness. Interestingly, however, in SnO_2|XTiO_2, the interplay of $\Delta H^{\ddagger}$ and $\Delta S^{\ddagger}$ result in nearly equal $\Delta G^{\ddagger}$ for all samples, 47 ± 3 kJ mol^{-1}. For both ZrO_2|XTiO_2 and SnO_2|XTiO_2, $\Delta G^{\ddagger}$ values predict the observed $k_{1/2}$ remarkably well (Fig. 10).

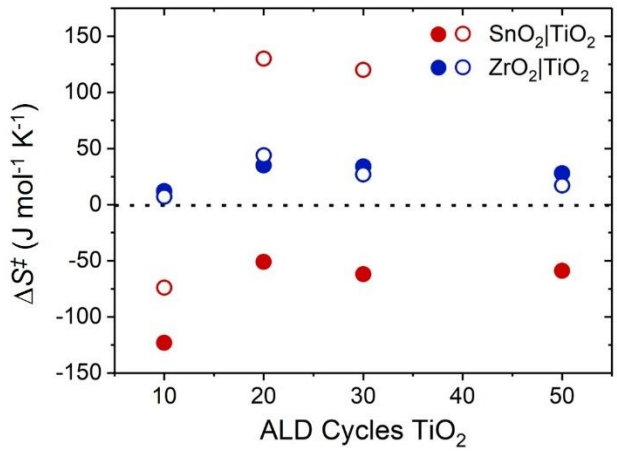

Figure 9. Values of $\Delta S^{\ddagger}$ for thermally-activated interfacial electron transfer on RuP-sensitized core|shell films in aqueous 0.1 M $HClO_4$. Each ALD cycle is estimated to deposit 0.66 Å TiO_2. Annealed materials, heated to 450 °C post TiO_2 deposition, are shown as solid circles, while unannealed materials, heated to only 200 °C, are shown as open circles. SnO_2|TiO_2 films are shown in red, while ZrO_2|TiO_2 films are shown in blue.

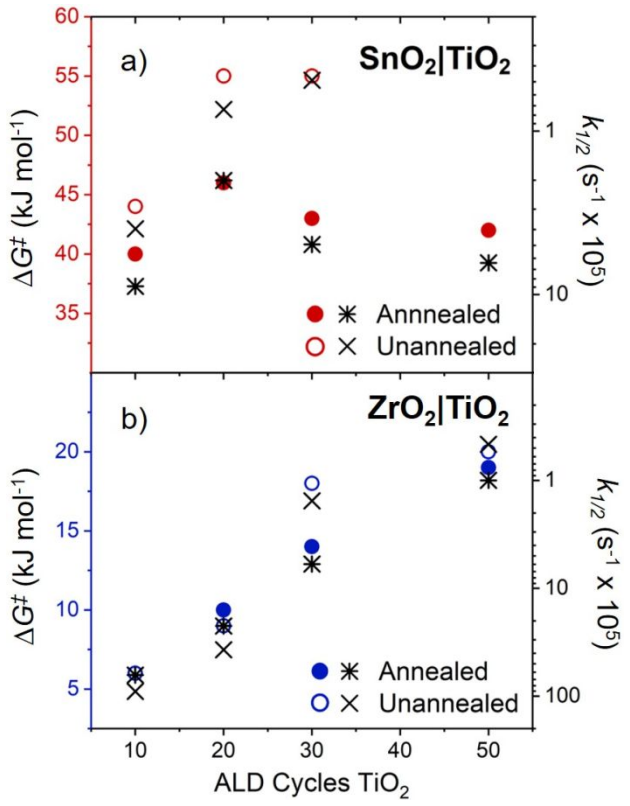

Figure 10. Comparative values of $\Delta G^{\ddagger}$ (linear scale, red or blue) and $k_{1/2}$ (log scale, black) for temperature-dependent interfacial ET in 0.1 M $HClO_4$ for RuP-sensitized a) $SnO_2|XTiO_2$ and b) $ZrO_2|XTiO_2$. Values observed at 60 °C are given, but similar agreement holds at all temperatures at which ET is thermally activated. Annealed materials are represented by closed circles ($\Delta G^{\ddagger}$) and asterisks ($k_{1/2}$). Unannealed materials are represented by open circles ($\Delta G^{\ddagger}$) and crosses ($k_{1/2}$).

Discussion

Interfacial electron transfer pseudo-rate constants $k_{1/2}$ were quantified as a function of temperature for RuP-sensitized mesoporous thin films of rutile SnO_2, anatase TiO_2 (*a*-TiO_2), rutile TiO_2 (*r*-TiO_2), $ZrO_2|XTiO_2$, and $SnO_2|XTiO_2$ (where X is the number of applied ALD cycles). For $SnO_2|XTiO_2$, the kinetic response varied dramatically between materials that were heated to 200 °C post TiO_2 deposition, termed 'unannealed', and materials that were heated to 450 °C, termed 'annealed'. While $k_{1/2}$ for annealed films increased exponentially with temperature, unannealed films exhibited $k_{1/2}$ values that were temperature-independent from 10 to 40 °C and increased exponentially at higher temperatures. For the thickest unannealed shells, $SnO_2|50TiO_2$, $k_{1/2}$ values were within experimental error equal across the entire probed temperature range, 10 to 80 °C.

Raman and HRTEM analysis indicate that, for $SnO_2|XTiO_2$, unannealed TiO_2 shells are likely amorphous, while annealed shells exhibit lattice fringes and Raman spectra consistent with the rutile polymorph, *r*-TiO_2. Because this morphology change appears to be associated with stark

differences in ET kinetics, these $SnO_2|XTiO_2$ materials lend an opportunity to develop a structure–function relationship between the crystallinity and the mechanism of interfacial electron transfer.

The temperature dependence of electron transfer kinetics differentiates thermally-activated and tunneling reactions.[62–64] For thermally-activated ET, rate constants are predicted to increase exponentially with temperature, as described by Eq. 3. Conversely, tunneling rate constants are predicted to be temperature independent, as described by Eq. 4, where $k°$ is the inherent electron transfer rate constant, β is the tunneling decay parameter, and D is the ET distance.

$$k = k° e^{-\beta D} \quad (4)$$

As such, an exponential temperature dependence of pseudo rate constants in this study indicates thermally-activated interfacial ET, while temperature independence denotes tunneling.

Thin TiO_2 Shells

Annealed and unannealed $ZrO_2|10TiO_2$ and $SnO_2|10TiO_2$ exhibit behavior distinct from analogous materials of the same type with thicker shells. Because these thin shells are not discernable in HRTEM images or Raman spectra, definitive morphology assignment is not possible. As such, meaningful structure function relationships cannot be unambiguously determined.

The kinetic results do reveal, however, that these thin-shell materials undergo faster ET than do materials with thicker shells. For annealed $SnO_2|10TiO_2$ and both annealed and unannealed $ZrO_2|10TiO_2$, values of $k_{1/2}$ increase exponentially with temperature, which indicates a thermally-activated ET. Unannealed $SnO_2|10TiO_2$, however, undergoes thermally-activated ET only at temperatures above ~ 40 °C, while at lower temperatures, ET occurs through tunneling. The fast ET kinetics in all thin-shell samples are consistent with small ET barriers signified by low E_a values. Additionally, they exhibit anomalously low (*i.e.* more negative) values of $\Delta S^{\ddagger}$, indicating transition states more entropically penalized than those in thicker shells. Annealed $SnO_2|10TiO_2$ exhibits an E_a within experimental error equal to both annealed and unannealed $ZrO_2|10TiO_2$ and SnO_2. This suggests annealed $SnO_2|10TiO_2$ may have a common ET rate determining step (RDS) with one or more of these materials, but evidence is inconclusive.

Annealed $SnO_2|XTiO_2$

Raman spectra and HRTEM images of annealed $SnO_2|XTiO_2$, where X is 20, 30, and 50, suggest that the TiO_2 shells have a rutile morphology. In these crystalline materials, values of $k_{1/2}$ increase exponentially with temperature from 10 to 80 °C, which shows that the RDS is exclusively thermally activated, with an activation energy of 30 $\pm$ 3 kJ mol^{-1} regardless of shell thickness. Importantly, this activation energy is only slightly larger than the E_a quantified for r-TiO_2 and annealed $ZrO_2|XTiO_2$, $E_a \approx 24$ kJ mol^{-1}. In $ZrO_2|XTiO_2$, the high energy acceptor states of the ZrO_2 core are inaccessible to electrons transferred from the RuP excited state. As such, annealed $ZrO_2|XTiO_2$ serves as a proxy for the behavior of the TiO_2 shell alone, albeit an imperfect one due

to its anatase crystallinity.[14] The discrepancy should be minimal, however, as equal E_a values were quantified for *a*- and *r*-TiO_2. The near parity of E_a between annealed $SnO_2|XTiO_2$, annealed $ZrO_2|XTiO_2$, and *r*-TiO_2 suggests a shared interfacial ET RDS.

The study of interfacial ET in dye-sensitized mesoporous TiO_2 materials has a long history,[65–67] much of which is concerned with determining the RDS and the physical source of the non-exponential kinetics.[57,68–70] Though far from conclusive,[71–73] under many experimental conditions, the observed rate constants report on transport of the injected electron to the oxidized sensitizer,[69,70,74] suggesting interfacial ET in TiO_2 to be rate limited by small polaron transport between $Ti^{III/IV}$ sites.[75] As such, the RDS for interfacial ET in annealed $SnO_2|XTiO_2$ is herein proposed to be electron $Ti^{III/IV}$ hopping, as shown in Scheme 2a. This is consistent with both the nearly equivalent E_a measured for annealed $SnO_2|XTiO_2$, annealed $ZrO_2|XTiO_2$, and *r*-TiO_2 and the lack of shell thickness dependence for E_a in annealed $SnO_2|XTiO_2$. It also does not preclude the possibility that electrons move between the SnO_2 and TiO_2 phases, as transport through SnO_2 is faster than that through TiO_2.[75]

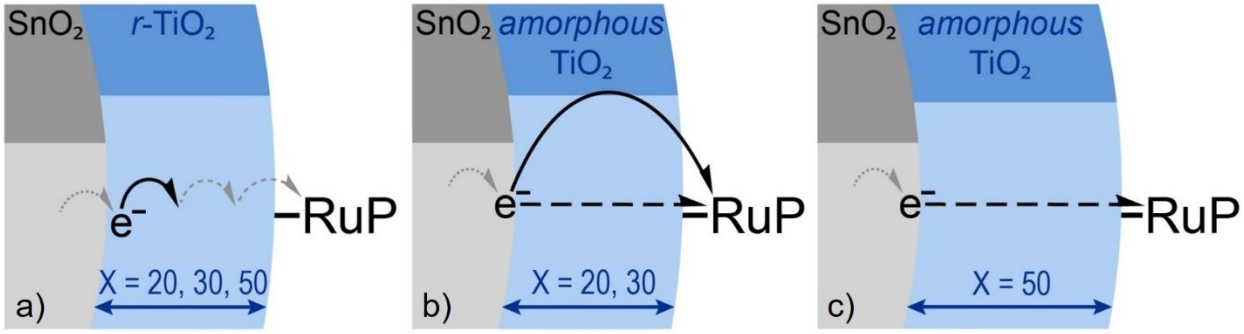

Scheme 2: Proposed interfacial electron transfer mechanisms in a) annealed and b-c) unannealed $SnO_2|XTiO_2$ in which X is the number of applied ALD cycles is X. Black arrows represent rate determining steps (RDS)—solid arrows are thermally activated and dashed are tunneling. Dashed gray arrows represent fast steps after an RDS, and gray dotted arrows indicate fast steps that may occur before the RDS. a) In annealed $SnO_2|XTiO_2$, HRTEM and Raman evidence suggest shells are rutile (*r*-TiO_2). Temperature-dependent kinetics are consistent with the RDS being thermally-activated $Ti^{III/IV}$ hopping through the shell. b-c) In unannealed $SnO_2|XTiO_2$, HRTEM and Raman evidence suggest shells are amorphous. b) When X = 20 and 30, temperature-dependent kinetics are consistent with tunneling from the core or interface to the RuP at low temperatures and activation into a conduction band-like transition state at high temperatures. c) When X = 50, temperature-independent kinetics are consistent with tunneling from the interface or core to the RuP.

Annealed $SnO_2|XTiO_2$ materials do, however, exhibit ET E_a values slightly larger than $ZrO_2|XTiO_2$ and *r*-TiO_2. Additionally, Eyring analysis reveals that $\Delta S^{\ddagger}$ for ET in annealed $SnO_2|XTiO_2$ is more negative than that of $ZrO_2|XTiO_2$, indicating a significant entropic penalty upon entering the transition state. Though the physical origin of this difference is not well-understood, it may reflect the chemical environment of the donor Ti^{III} in the $Ti^{III/IV}$ hop. If the donor Ti^{III} in the RDS is in or near the SnO_2/TiO_2 interface, lattice distortions may lead to a disordered reagent state, and thus the observed entropic cost in the transition state.

Unannealed $SnO_2|XTiO_2$

Unannealed $SnO_2|XTiO_2$ materials exhibit starkly different temperature-dependent kinetics than do their annealed counterparts. Raman spectra and HRTEM images of unannealed $SnO_2|XTiO_2$, where X is 20, 30, and 50, suggest the TiO_2 shells to be amorphous. For the thickest unannealed shells, $SnO_2|50TiO_2$, temperature-independent $k_{1/2}$ values from 10 to 80 °C indicate that interfacial ET occurs exclusively through tunneling. Tunneling is also indicated in unannealed $SnO_2|20TiO_2$ and $SnO_2|30TiO_2$ at temperatures below 40 °C. At higher temperatures, however, the $k_{1/2}$ values accelerate rapidly with temperature as a thermally-activated ET mechanism with a remarkably large barrier, $E_a \approx 95$ kJ mol^{-1}, eclipses the tunneling reaction.

These data reveal that, for $SnO_2|XTiO_2$ materials, the post-deposition heat treatment and resulting shell morphology determine the operative interfacial ET mechanism. The amorphous TiO_2 shell alone, however, is not sufficient to account for the tunneling and large ET barriers in unannealed $SnO_2|XTiO_2$. Though Raman and HRTEM evidence suggest that unannealed $ZrO_2|20/30TiO_2$ and $ZrO_2|Al_2O_3|50TiO_2$ have amorphous shells, these materials undergo exclusively thermally-activated ET, unlike the $SnO_2|XTiO_2$ materials. In fact, for ZrO_2 with amorphous TiO_2 shells, $k_{1/2}$ and E_a values were within experimental error equal to those of annealed $ZrO_2|XTiO_2$ with anatase shells. This barrier $E_a \approx 24$ kJ mol^{-1} is in stark contrast to unannealed $SnO_2|20/30TiO_2$, where an incredibly large barrier exists that cannot be overcome at low temperatures. As such, the RDS for interfacial ET in unannealed $SnO_2|XTiO_2$ cannot be $Ti^{III/IV}$ hopping, nor is it easily rationalized by any mechanism that invokes only the amorphous TiO_2 shell. The RDS must instead involve either the SnO_2 core or the SnO_2/TiO_2 interface.

The RDS of thermally-activated ET in unannealed $SnO_2|XTiO_2$ is highly entropically favored, with $\Delta S^{\ddagger} \approx 125$ J mol^{-1} K^{-1}. This large positive $\Delta S^{\ddagger}$ value indicates the transition state to be significantly more disordered than the reactant state. A highly energetic and highly disordered transition state is consistent with activation into or near the delocalized TiO_2 conduction band. It is plausible that this activation results in ET into the amorphous TiO_2, and the electron then undergoes comparatively fast $Ti^{III/IV}$ hopping to the $Ru^{III}P$ acceptor. This mechanism, however, is inconsistent with the changeover from large-barrier thermally-activated ET in unannealed $SnO_2|20/30TiO_2$ to tunneling at all temperatures in unannealed $SnO_2|50TiO_2$. Instead, it is proposed that thermally-activated interfacial ET in unannealed $SnO_2|20/30TiO_2$ occurs in one step—an electron moves directly from the core or interface to the $Ru^{III}P$ through a conduction-band like transition state.

In total, this data suggests a physical picture of interfacial ET in unannealed $SnO_2|XTiO_2$ (Scheme 2) in which electron movement from the core or interface into the amorphous TiO_2 is associated with a prohibitively large energetic barrier. This is consistent with recent findings that electron transport in a $SnO_2|XTiO_2$-based dye-sensitized solar cell occurs through TiO_2 when the material is annealed but SnO_2 when the material is unannealed.[21] At low temperatures, electrons in unannealed $SnO_2|XTiO_2$ tunnel from either the core or core/shell interface to the $Ru^{III}P$ sensitizer. At higher temperatures, the rate constant for thermally-activated ET from the core or

interface to the $Ru^{III}P$ becomes faster than the tunneling process and thus predominates. This mechanistic change is able to occur at a relatively low temperature, ~ 40 °C, despite a massive activation barrier due to the entropic favorability of a delocalized conduction band-like transition state. In materials with very thick amorphous shells ($SnO_2|50TiO_2$), however, the distance between the core or interface and the $Ru^{III}P$ is too great to cover in a single activated step, and ET occurs exclusively through tunneling.

Informing a Predictive Model

Here, the thickness and morphology of the TiO_2 shell in a $SnO_2|TiO_2$ core|shell nanostructure was found to determine the mechanism by which the material underwent interfacial electron transfer with a surface-anchored molecule. Control of the shell thickness and morphology should thus allow predictable control of the interfacial ET rate constant and help realize the specific goal of slowing undesirable charge recombination in core|shell nanostructures utilized for solar energy conversion.

In both annealed and unannealed $SnO_2|XTiO_2$, interfacial ET was observed to be thermally activated under at least some conditions. Despite that thermally-activated ET in annealed and unannealed $SnO_2|XTiO_2$ seem to have different RDSs, the reactions occur with similar Gibbs activation energies. In unannealed $SnO_2|XTiO_2$, the interplay of large enthalpic barriers and significant entropic incentives results in $\Delta G^{\ddagger}$ values only slightly larger than those of the annealed $SnO_2|XTiO_2$. This similarity in $\Delta G^{\ddagger}$ results in unannealed $SnO_2|20/30TiO_2$ manifesting interfacial ET $k_{1/2}$ values less than an order of magnitude smaller than those of the annealed materials (Fig. 10).

The smasllest attainable $k_{1/2}$ values are instead achieved by promoting a tunneling mechanism, especially at the elevated temperatures at which terrestrial solar energy conversion devices operate. The structure/function relationship between the shell morphology and the ET mechanism thus becomes instructive. To create a system in which electrons will reliably tunnel, shells must be amorphous and sufficiently thick to disallow a thermally-activated direct electron transfer from the core or interface to the molecular acceptor.

The kinetic data in this study suggest that electron transfer between a crystalline core or the nearby core|shell interface and an amorphous shell may be prohibitively difficult. The physical reason, however is not readily apparent from these results. Electron transfer between rutile SnO_2 and amorphous TiO_2 could be constrained by the difficulty of increasing the effective mass of the electron, of a large polaron becoming a small polaron, or of moving from an s to a d orbital between which coupling is poor. Currently, however, the acceptor states of $SnO_2|XTiO_2$ materials are not well characterized. A better understanding of the electron dynamics within $SnO_2|TiO_2$ and other core|shell nanostructures is necessary to clarify the details of their interfacial electron transfer mechanisms.

Conclusions

This study represents a significant step forward in elucidating detailed mechanistic information on interfacial electron transfer in $SnO_2|TiO_2$ core|shell nanostructures to molecular acceptors at the TiO_2 shell surface. Temperature dependent kinetic studies have definitively shown that both tunneling and thermally-activated electron transfer are operative in sensitized $SnO_2|TiO_2$ materials. Most notably, the mechanism of interfacial electron transfer depends critically on the temperature to which the $SnO_2|TiO_2$ is heated after TiO_2 deposition. High annealing temperatures result in rutile TiO_2 shells and thermally-activated electron transfer proposed herein to be rate limited by $Ti^{III/IV}$ hopping in the shell. Low annealing temperatures result in amorphous TiO_2 shells and a kinetic competition between tunneling and thermally-activated interfacial electron transfer. Here, remarkably large activation energies are offset by entropically favorable transition states. Ultimately, the interplay of entropic and enthalpic barriers reliably predicts the interfacial electron transfer pseudo-rate constants of each sensitized material. The slowest interfacial electron transfer is achieved in thick amorphous shells and occurs by a tunneling mechanism.

Experimental

Electrode Materials and Fabrication

Sol-gel pastes of SnO_2, ZrO_2, anatase TiO_2 (*a*-TiO_2), and rutile TiO_2 (*r*-TiO_2) were synthesized through previously reported methods with slight modifications.[26–28] Detailed procedures are given in Supplemental Information (SI). Thin films were fabricated by doctor-blading a metal oxide paste onto clean fluorine-doped tin oxide glass plates (FTO, Hartford Glass, 15 Ω/sq) or glass microscope slides, using a layer of Scotch tape as a spacer. After drying in air, films were heated to at least 450 °C for 30-60 minutes. Exact heating conditions are given in SI. The films then immediately underwent either atomic layer deposition or dye-loading. Films thicknesses were measured by a Bruker Optics DektakXT stylus profilometer as follows: SnO_2 was 4-6 μm, ZrO_2 was 5-7 μm, *a*-TiO_2 was 4 μm, and *r*-TiO_2 was 5-6 μm.

Atomic Layer Deposition (ALD) of TiO_2 Shells

Atomic layer deposited coatings were fabricated using an Ultratech/Cambridge NanoTech Savannah S200 reactor system. Tetrakisdimethylamidotitanium(IV) (TDMA-Ti) (Sigma-Aldrich, 99.999%) and ultrapure DI water served as the reactant and co-reactant for the deposition of TiO_2, each equilibrated at 75 °C for 1 hour prior to deposition. Ultrahigh purity N_2 (Airgas, 99.999%) served as the carrier gas. The empty ALD chamber was pre-treated with 50 cycles of TiO_2 deposited at 150 °C to ensure a consistent sticking coefficient to the reactor walls. Metal oxide films annealed on FTO were aligned parallel to the inlet and outlet ports, and the chamber was placed under dynamic vacuum for 10 minutes with a carrier gas flow rate of 20 sccm. Prior to precursor exposure, the chamber was isolated from dynamic vacuum, which was resumed during the purge steps. One ALD cycle consisted of a 0.5 sec dose of TDMA-Ti, 20 sec exposure, 30 sec purge, 0.02 sec dose of H_2O, 20 sec exposure, and 30 sec purge. The flow rate was reduced to 5 sccm prior to precursor doses and increased to 400 sccm during purges. The thickness of the shell was controlled by the number of applied ALD cycles. After ALD, the core|shell films were immediately heat treated for 30 min (225 °C/hr ramp-up, 450 °C/hr ramp-down). Core|shell films termed "unannealed" were treated at 200 °C, and films termed "annealed" were heated at 450 °C.

Herein, shell thicknesses are described in terms of the number of ALD cycles of TiO_2 rather than a geometric thickness to avoid mischaracterizing inhomogeneous shells. For the sake of comparison, the TiO_2 ALD in this study has been estimated from transmission electron microscopy to deposit 0.66 Å per cycle, similar to the per-cycle deposition measured by ellipsometry on planar silicon wafers previously.[14,21]

Dye Loading

Metal oxide materials were sensitized to the maximum attainable surface coverage by reaction with 6 mM [Ru(2,2′-bipyridine)$_2$(4,4′-bis(phosphonic acid)-2,2′-bipyridine)]$^{2+}$, abbreviated RuP, in methanol for 24 hours. The synthesis of RuP has been discussed previously.[29]

Film Characterization

Raman spectra were acquired using a Renishaw inVia Raman spectrophotometer equipped with a Leica microscope. The 633 nm excitation source was generated by a RenishawRL633 HeNe laser. The Raman shift was calibrated to the silicon F_{1g} peak (520.2 ± 0.2 cm^{-1}). 20 accumulative measurements were performed for each sample in the dark using a 1800 I/mm (vis) grating, a CCD camera detector, and a 10 second exposure time.

High resolution transmission electron microscopy (HRTEM) imaging was performed using a FEI Talos F200X transmission electron microscope which applied an accelerating voltage of 200 kV. Samples were stripped from glass microscope slides using an electron microscopy razor blade, and the powder was sonicated for 20 minutes in ethanol. The resulting dispersions were drop-cast onto 400 mesh lacey carbon grids and dried under vacuum. All images were analyzed in ImageJ software. Lattice space (d-space) values were quantified by averaging at least 10 measurements obtained from the fast-Fourier transform (FFT) of a selected area of the image. If necessary, for some samples a circular mask was applied to two diffraction points and d-space values were obtained from the inverse FFT.

UV–visible absorbance spectra were obtained on an Agilent Cary 60 UV–vis spectrophotometer. The films were immersed in N_2-sparged 0.1 M $HClO_4$ aqueous solutions and held at 45° relative to the incident light.

Transient Absorption Spectroscopy

Transient absorption spectroscopy in N_2-sparged 0.1 M aqueous $HClO_4$ was performed using a previously described apparatus.[30] Pulsed light excitation was enacted with a Q-switched, pulsed Nd:YAG laser doubled to 532 nm (Quantel, U.S.A., Brilliant B, 5-6 nm FWHM). Samples were excited at 1 Hz with laser fluence at the sample of ~ 3 mJ/pulse. Absorption changes were probed by a 150 W xenon arc lamp aligned perpendicular to the pulse beam. The probe lamp was pulsed to 70 V at 1 Hz for time scales < 100 μs. Light detection was accomplished with a SPEX 1702/04 monochromator optically coupled to a photomultiplier tube (Hamamatsu R928) connected to a digital oscilloscope (LeCroy 9450, Dual 330 MHz). The overall instrument response time was ~ 10 ns. Single wavelength kinetics are presented as an average of 90-150 laser pulses. Transient absorption spectroscopy was performed as a function of sample temperature, 10 °C to 80 °C, which was controlled with a CoolSpek cryostat (Unisoku).

Associated Content

The Supporting Information contains

metal oxide sol-gel paste synthesis procedures, Raman spectra, HRTEM images, XRD spectra, UV-visible absorption spectra, transient absorption kinetics, BET rate constants as a function of shell thickness, Eyring analysis

Acknowledgements

The authors would like to thank Dr. Erica M. James for thoughtful conversations. This material is based upon work solely supported by the Alliance for Molecular PhotoElectrode Design for Solar Fuels (AMPED), an Energy Frontier Research Center (EFRC) funded by the U.S. Department of Energy, Office of Science, Office of Basic Energy Sciences under Award Number DE-SC0001011. REB acknowledges the National Science Foundation for an individual Graduate Research Fellowship under Grant No. DGE-1650116. This work was performed in part using instrumentation at the Chapel Hill Analytical and Nanofabrication Laboratory, CHANL, a member of the North Carolina Research Triangle Nanotechnology Network, RTNN, which is supported by the National Science Foundation, Grant ECCS- 1542015, as part of the National Nanotechnology Coordinated Infrastructure, NNCI. This work was performed in part at the Analytical Instrumentation Facility (AIF) at North Carolina State University, which is supported by the State of North Carolina and the National Science Foundation (award number ECCS-1542015). This work made use of instrumentation at AIF acquired with support from the National Science Foundation (DMR-1726294). The AIF is a member of the North Carolina Research Triangle Nanotechnology Network (RTNN), a site in the National Nanotechnology Coordinated Infrastructure (NNCI).

References

(1) Li, W.; Elzatahry, A.; Aldhayan, D.; Zhao, D. Core-Shell Structured Titanium Dioxide Nanomaterials for Solar Energy Utilization. *Chem. Soc. Rev.* **2018**, *47* (22), 8203–8237.

(2) Brennaman, M. K.; Dillon, R. J.; Alibabaei, L.; Gish, M. K.; Dares, C. J.; Ashford, D. L.; House, R. L.; Meyer, G. J.; Papanikolas, J. M.; Meyer, T. J. Finding the Way to Solar Fuels with Dye-Sensitized Photoelectrosynthesis Cells. *J. Am. Chem. Soc.* **2016**, *138*, 13085–13102.

(3) Prasittichai, C.; Hupp, J. T. Surface Modification of SnO_2 Photoelectrodes in Dye-Sensitized Solar Cells: Significant Improvements in Photovoltage via Al_2O_3 Atomic Layer Deposition. *J. Phys. Chem. Lett.* **2010**, *1* (10), 1611–1615.

(4) Miller, D. R.; Akbar, S. A.; Morris, P. A. Nanoscale Metal Oxide-Based Heterojunctions for Gas Sensing: A Review. *Sensors Actuators, B Chem.* **2014**, *204*, 250–272.

(5) Idota, Y.; Kubota, T.; Matsufuji, A.; Maekawa, Y.; Miyasaka, T. Tin-Based Amorphous Oxide: A High-Capacity Lithium-Ion-Storage Material. *Science.* **1997**, *276* (5317), 1395–1397.

(6) Su, L.; Jing, Y.; Zhou, Z. Li Ion Battery Materials with Core-Shell Nanostructures. *Nanoscale* **2011**, *3* (10), 3967–3983.

(7) Liu, P.; Wang, C.; Zhou, D.; Yuan, Q.; Wang, Y.; Hu, Y.; Han, D.; Feng, L. WO_x@PEDOT Core-Shell Nanorods: Hybrid Hole-Transporting Materials for Efficient and Stable Perovskite Solar Cells. *ACS Appl. Energy Mater.* **2018**, *1* (4), 1742–1752.

(8) Pang, A.; Sun, X.; Ruan, H.; Li, Y.; Dai, S.; Wei, M. Highly Efficient Dye-Sensitized Solar Cells Composed of TiO_2@SnO_2 Core-Shell Microspheres. *Nano Energy* **2014**, *5*, 82–90.

(9) Wee, K. R.; Sherman, B. D.; Brennaman, M. K.; Sheridan, M. V.; Nayak, A.; Alibabaei, L.; Meyer, T. J. An Aqueous, Organic Dye Derivatized SnO_2/TiO_2 Core/Shell Photoanode. *J. Mater. Chem. A* **2016**, *4* (8), 2969–2975.

(10) Wang, D.; Wang, L.; Brady, M. D.; Dares, C. J.; Meyer, G. J.; Meyer, T. J.; Concepcion, J. J. Self-Assembled Chromophore−Catalyst Bilayer for Water Oxidation in a Dye-Sensitized Photoelectrosynthesis Cell. *J. Phys. Chem. C* **2019**, *123*, 30039–30045.

(11) Karlsson, M.; Jõgi, I.; Eriksson, S. K.; Rensmo, H.; Boman, M.; Boschloo, G.; Hagfeldt, A. Dye-Sensitized Solar Cells Employing a SnO_2-TiO_2 Core-Shell Structure Made by Atomic Layer Deposition. *Chimia (Aarau).* **2013**, *67* (3), 142–148.

(12) Alibabaei, L.; Farnum, B. H.; Kalanyan, B.; Brennaman, M. K.; Losego, M. D.; Parsons, G. N.; Meyer, T. J. Atomic Layer Deposition of TiO_2 on Mesoporous NanoITO: Conductive Core-Shell Photoanodes for Dye-Sensitized Solar Cells. *Nano Lett* **2014**, *14*, 3255–3261.

(13) Sherman, B. D.; Ashford, D. L.; Lapides, A. M.; Sheridan, M. V; Wee, K.-R.; Meyer, T. J. Light-Driven Water Splitting with a Molecular Electroassembly-Based Core/Shell Photoanode. *J. Phys. Chem. Lett* **2015**, *6*, 3213–3217.

(14) Knauf, R. R.; Kalanyan, B.; Parsons, G. N.; Dempsey, J. L. Charge Recombination Dynamics in Sensitized SnO_2/TiO_2 Core/Shell Photoanodes. *J. Phys. Chem. C* **2015**, *119*, 28353–28360.

(15) Prasittichai, C.; Avila, J. R.; Farha, O. K.; Hupp, J. T. Systematic Modulation of Quantum (Electron) Tunneling Behavior by Atomic Layer Deposition on Nanoparticulate SnO_2 and TiO_2 Photoanodes. *J. Am. Chem. Soc.* **2013**, *135* (44), 16328–16331.

(16) Avila, J. R.; Katz, M. J.; Farha, O. K.; Hupp, J. T. Barrier-Layer-Mediated Electron Transfer from Semiconductor Electrodes to Molecules in Solution: Sensitivity of Mechanism to Barrier-Layer Thickness. *J. Phys. Chem. C* **2016**, *120* (1), 20922–20928.

(17) Gish, M. K.; Lapides, A. M.; Brennaman, M. K.; Templeton, J. L.; Meyer, T. J.; Papanikolas, J. M. Ultrafast Recombination Dynamics in Dye-Sensitized SnO_2/TiO_2 Core/Shell Films. *J. Phys. Chem. Lett.* **2016**, *7* (24), 5297–5301.

(18) Cao, F.; Oskam, G.; Searson, P. C.; Stipkala, J. M.; Heimer, T. A.; Farzad, F.; Meyer, G. J. Electrical and Optical Properties of Porous Nanocrystalline TiO_2 Films. *J. Phys. Chem.* **1995**, *99* (31), 11974–11980.

(19) Moehl, T.; Suh, J.; Sévery, L.; Wick-Joliat, R.; Tilley, S. D. Investigation of (Leaky) ALD TiO_2 Protection Layers for Water-Splitting Photoelectrodes. *ACS Appl. Mater. Interfaces* **2017**, *9* (50), 43614–43622.

(20) Castillo-Lora, J.; Mitsuhashi, R.; Mayer, J. M. Revealing the Relative Electronic Landscape of Colloidal ZnO and TiO_2 Nanoparticles via Equilibration Studies. *J. Phys. Chem. C* **2019**, *123* (16), 10262–10271.

(21) James, E. M.; Bennett, M. T.; Bangle, R. E.; Meyer, G. J. Electron Localization and Transport in SnO_2/TiO_2 Mesoporous Thin Films: Evidence for a $SnO_2/Sn_xTi_{1-x}O_2/TiO_2$ Structure. *Langmuir* **2019**, *35* (39), 12694–12703.

(22) James, E. M.; Barr, T. J.; Meyer, G. J. Evidence for an Electronic State at the Interface between the SnO_2 Core and the TiO_2 Shell in Mesoporous SnO_2/TiO_2 Thin Films. *ACS Appl. Energy Mater.* **2018**, *1* (2), 859–867.

(23) Trotochaud, L.; Boettcher, S. W. Synthesis of Rutile-Phase $Sn_xTi_{1-x}O_2$ Solid-Solution and $(SnO_2)_x/(TiO_2)_{1-x}$ Core/Shell Nanoparticles with Tunable Lattice Constants and Controlled Morphologies. *Chem. Mater.* **2011**, *23* (22), 4920–4930.

(24) Green, A. N. M.; Palomares, E.; Haque, S. A.; Kroon, J. M.; Durrant, J. R. Charge Transport versus Recombination in Dye-Sensitized Solar Cells Employing Nanocrystalline TiO_2 and SnO_2 Films. *J. Phys. Chem. B* **2005**, *109*, 12525–12533.

(25) Mathew, S.; Yella, A.; Gao, P.; Humphry-Baker, R.; E Curchod, B. F.; Ashari-Astani, N.; Tavernelli, I.; Rothlisberger, U.; Khaja Nazeeruddin, M.; Grätzel, M. Dye-Sensitized Solar Cells with 13% Efficiency Achieved through the Molecular Engineering of Porphyrin Sensitizers. *Nat. Chem.* **2014**, *6*, 242–247.

(26) Mortelliti, M. J.; Wang, A. N.; Dempsey, J. L. Atomic Layer Deposition of SnO_x onto Mesoporous, Nanocrsytalline TiO_2 and SnO_2 Thin Films. *Polyhedron* **2019**, *171*, 433–437.

(27) Heimer, T. A.; D'Arcangelis, S. T.; Farzad, F.; Stipkala, J. M.; Meyer, G. J. An Acetylacetonate-Based Semiconductor−Sensitizer Linkage. *Inorg. Chem.* **1996**, *35* (18), 5319–5324.

(28) Swierk, J. R.; Regan, K. P.; Jiang, J.; Brudvig, G. W.; Schmuttenmaer, C. A. Rutile TiO_2 as an Anode Material for Water-Splitting Dye-Sensitized Photoelectrochemical Cells. *ACS Energy Lett.* **2016**, *1* (3), 603–606.

(29) Norris, M. R.; Concepcion, J. J.; Glasson, C. R. K.; Fang, Z.; Lapides, A. M.; Ashford, D. L.; Templeton, J. L.; Meyer, T. J. Synthesis of Phosphonic Acid Derivatized Bipyridine Ligands and Their Ruthenium Complexes. *Inorg. Chem.* **2013**, *52* (21), 12492–12501.

(30) Argazzi, R.; Bignozzi, C. A.; Heimer, T. A.; Castellano, F. N.; Meyer, G. J. Enhanced Spectral Sensitivity from Ruthenium(II) Polypyridyl Based Photovoltaic Devices. *Inorg. Chem.* **1994**, *33*, 5741–5749.

(31) Dendooven, J.; Goris, B.; Devloo-Casier, K.; Levrau, E.; Biermans, E.; Baklanov, M. R.; Ludwig, K. F.; Voort, P. Van Der; Bals, S.; Detavernier, C. Tuning the Pore Size of Ink-Bottle Mesopores by Atomic Layer Deposition. *Chem. Mater.* **2012**, *24* (11), 1992–1994.

(32) Dendooven, J.; Devloo-Casier, K.; Ide, M.; Grandfield, K.; Kurttepeli, M.; Ludwig, K. F.; Bals, S.; Van Der Voort, P.; Detavernier, C. Atomic Layer Deposition-Based Tuning of the Pore Size in Mesoporous Thin Films Studied by in Situ Grazing Incidence Small Angle X-Ray Scattering. *Nanoscale* **2014**, *6* (24), 14991–14998.

(33) Dendooven, J.; Pulinthanathu Sree, S.; De Keyser, K.; Deduytsche, D.; Martens, J. A.; Ludwig, K. F.; Detavernier, C. In Situ X-Ray Fluorescence Measurements during Atomic Layer Deposition: Nucleation and Growth of TiO_2 on Planar Substrates and in Nanoporous Films. *J. Phys. Chem. C* **2011**, *115* (14), 6605–6610.

(34) Liu, L. Z.; Xu, J. Q.; Wu, X. L.; Li, T. H.; Shen, J. C.; Chu, P. K. Optical Identification of Oxygen Vacancy Types in SnO_2 Nanocrystals. *Appl. Phys. Lett.* **2013**, *102* (3), 1–5.

(35) Zuo, J.; Xu, C.; Liu, X.; Wang, C.; Wang, C.; Hu, Y.; Qian, Y. Study of the Raman Spectrum of Nanometer SnO_2. *J. Appl. Phys.* **1994**, *75* (3), 1835–1836.

(36) Abello, L.; Bochu, B.; Gaskov, A.; Koudryavtseva, S.; Lucazeau, G.; Roumyantseva, M. Structural Characterization of Nanocrystalline SnO_2 by X-Ray and Raman Spectroscopy. *J. Solid State Chem.* **1998**, *135* (1), 78–85.

(37) Diéguez, A.; Romano-Rodríguez, A.; Vilà, A.; Morante, J. R. The Complete Raman Spectrum of Nanometric SnO_2 Particles. *J. Appl. Phys.* **2001**, *90* (3), 1550–1557.

(38) Song, M.; Wu, Y.; Zhao, Y.; Du, C.; Su, Y. Structural Insight on Defect-Rich Tin Oxide for Smart Band Alignment Engineering and Tunable Visible-Light-Driven Hydrogen Evolution. *Inorg. Chem.*

(39) Batzill, M.; Diebold, U. The Surface and Materials Science of Tin Oxide. *Prog. Surf. Sci.* **2005**, *79* (2–4), 47–154.

(40) Geurts, J.; Rau, S.; Richter, W.; Schmitte, F. J. SnO Films and Their Oxidation to SnO_2: Raman Scattering, IR Reflectivity and X-Ray Diffraction Studies. *Thin Solid Films* **1984**, *121* (3), 217–225.

(41) Ma, H. L.; Yang, J. Y.; Dai, Y.; Zhang, Y. B.; Lu, B.; Ma, G. H. Raman Study of Phase Transformation of TiO_2 Rutile Single Crystal Irradiated by Infrared Femtosecond Laser. *Appl. Surf. Sci.* **2007**, *253* (18), 7497–7500.

(42) Frank, O.; Zukalova, M.; Laskova, B.; Kürti, J.; Koltai, J.; Kavan, L. Raman Spectra of Titanium Dioxide (Anatase, Rutile) with Identified Oxygen Isotopes (16, 17, 18). *Phys. Chem. Chem. Phys.* **2012**, *14* (42), 14567–14572.

(43) Lee, W.-J.; Hon, M.-H. Space-Limited Crystal Growth Mechanism of TiO_2 Films by Atomic Layer Deposition. *J. Phys. Chem. C* **2010**, *114*, 6917–6921.

(44) Aarik, J.; Aidla, A.; Uustare, T.; Sammelselg, V. Morphology and Structure of TiO_2 Thin Films Grown by Atomic Layer Deposition. *J. Cryst. Growth* **1995**, *148* (3), 268–275.

(45) Miikkulainen, V.; Leskelä, M.; Ritala, M.; Puurunen, R. L. Crystallinity of Inorganic Films Grown by Atomic Layer Deposition: Overview and General Trends. *J. Appl. Phys.* **2013**, *113* (2).

(46) Nie, A.; Liu, J.; Li, Q.; Cheng, Y.; Dong, C.; Zhou, W.; Wang, P.; Wang, Q.; Yang, Y.; Zhu, Y.; Zeng, Y.; Wang, H. Epitaxial TiO_2/SnO_2 Core-Shell Heterostructure by Atomic Layer Deposition. *J. Mater. Chem.* **2012**, *22* (21), 10665–10671.

(47) Wang, H.; Xu, S.; Gordon, R. G. Low Temperature Epitaxial Growth of High Permittivity Rutile TiO_2 on SnO_2. *Electrochem. Solid-State Lett.* **2010**, *13* (9), G75–G78.

(48) Pezzotti, G.; Porporati, A. A. Raman Spectroscopic Analysis of Phase-Transformation and Stress Patterns in Zirconia Hip Joints. *J. Biomed. Opt.* **2004**, *9* (2), 372–384.

(49) Naumenko, A.; Gnatiuk, I.; Smirnova, N.; Eremenko, A. Characterization of Sol–Gel Derived TiO_2/ZrO_2 Films and Powders by Raman Spectroscopy. *Thin Solid Films* **2012**, *520*, 4541–4546.

(50) Azough, F.; Freer, R.; Petzelt, J. A Raman Spectral Characterization of Ceramics in the System ZrO_2-TiO_2. *J. Mater. Sci.* **1993**, *28*, 2273–2276.

(51) Krebs, M. A.; Condrate Sr, R. A. A Raman Spectral Characterization of Various Crystalline Mixtures in the ZrO_2-TiO_2 and HfO_2-TiO_2 Systems. *J. Mater. Sci. Lett.* **1988**, *7*, 1327–1330.

(52) George, A.; Solomon, S.; Thomas, J. K.; John, A. Characterizations and Electrical Properties of $ZrTiO_4$ Ceramic. *Mater. Res. Bull.* **2012**, *47*, 3141–3147.

(53) Lucena, P. R. De; Leite, E. R.; Pontes, F. M.; Longo, E.; Pizani, P. S.; Varela, J. A. Photoluminescence: A Probe for Short, Medium and Long-Range Self-Organization Order in $ZrTiO_4$ Oxide. *J. Solid State Chem.* **2006**, *179*, 3997–4002.

(54) Kim, Y. K.; Jang, H. M. Raman Line-Shape Analysis of Nano-Structural Evolution in Cation-Ordered $ZrTiO_4$-Based Dielectrics. *Solid State Commun.* **2003**, *127*, 433–437.

(55) Brady, M. D.; Troian-Gautier, L.; Sampaio, R. N.; Motley, T. C.; Meyer, G. J. Optimization of Photocatalyst Excited- and Ground-State Reduction Potentials for Dye-Sensitized HBr Splitting. *ACS Appl. Mater. Interfaces* **2018**, *10* (37), 31312–31323.

(56) Knauf, R. R.; Brennaman, M. K.; Alibabaei, L.; Norris, M. R.; Dempsey, J. L. Revealing the Relationship between Semiconductor Electronic Structure and Electron Transfer Dynamics at Metal Oxide-Chromophore Interfaces. *J. Phys. Chem. C* **2013**, *117*, 25259–25268.

(57) Nelson, J.; Chandler, R. E. Random Walk Models of Charge Transfer and Transport in Dye Sensitized Systems. *Coord. Chem. Rev.* **2004**, *248*, 1181–1194.

(58) Haque, S. A.; Tachibana, Y.; Willis, R. L.; Moser, J. E.; Grätzel, M.; Klug, D. R.; Durrant, J. R. Parameters Influencing Charge Recombination Kinetics in Dye-Sensitized Nanocrystalline Titanium Dioxide Films. *J. Phys. Chem. B* **2000**, *104*, 538–547.

(59) Jakschik, S.; Schroeder, U.; Hecht, T.; Bartha, J. W.; Gutsche, M.; Seidl, H. Crystallization Behavior of Thin ALD-Al_2O_3 Films. *Thin Solid Films* **2003**, *425*, 216–220.

(60) Troian-Gautier, L.; Sampaio, R. N.; Piechota, E. J.; Brady, M. D.; Meyer, G. J. Barriers for Interfacial Back-Electron Transfer: A Comparison between TiO_2 and SnO_2/TiO_2

Core/Shell Structures. *J. Chem. Phys.* **2019**, *150*, 041719.

(61) Troian-Gautier, L.; DiMarco, B. N.; Sampaio, R. N.; Marquard, S. L.; Meyer, G. J. Evidence That $\Delta S^{\ddagger}$ Controls Interfacial Electron Transfer Dynamics from Anatase TiO_2 to Molecular Acceptors. *J. Am. Chem. Soc.* **2018**, *140* (8), 3019–3029.

(62) Hines, T.; Diez-Perez, I.; Hihath, J.; Liu, H.; Wang, Z.-S.; Zhao, J.; Zhou, G.; Müllen, K.; Tao, N. Transition from Tunneling to Hopping in Single Molecular Junctions by Measuring Length and Temperature Dependence. *J. Am. Chem. Soc.* **2010**, *132* (33), 11658–11664.

(63) Weiss, E. A.; Tauber, M. J.; Kelley, R. F.; Ahrens, M. J.; Ratner, M. A.; Wasielewski, M. R. Conformationally Gated Switching between Superexchange and Hopping within Oligo-p-Phenylene-Based Molecular Wires. *J. Am. Chem. Soc.* **2005**, *127*, 11842–11850.

(64) Katoh, R.; Furube, A. Tunneling-Type Charge Recombination in Nanocrystalline TiO_2 Films at Low Temperature. *J. Phys. Chem. Lett.* **2011**, *2* (15), 1888–1891.

(65) Huang, S. Y.; Schlichtho, G.; Nozik, A. J.; Gratzel, M.; Frank, A. J. Charge Recombination in Dye-Sensitized Nanocrystalline TiO_2 Solar Cells. *J. Phys. Chem. B* **1997**, *101* (14), 2576–2582.

(66) Hagfeldt, A.; Boschloo, G.; Sun, L.; Kloo, L.; Pettersson, H. Dye-Sensitized Solar Cells. *Chem. Rev.* **2010**, *110*, 6595–6663.

(67) Ardo, S.; Meyer, G. J. Photodriven Heterogeneous Charge Transfer with Transition-Metal Compounds Anchored to TiO_2 Semiconductor Surfaces. *Chem. Soc. Rev.* **2009**, *38* (1), 115–164.

(68) Ghosh, H. N.; Asbury, J. B.; Weng, Y.; Lian, T. Interfacial Electron Transfer between $Fe(II)(CN)_6^{4-}$ and TiO_2 Nanoparticles: Direct Electron Injection and Nonexponential Recombination. *J. Phys. Chem. B* **1998**, *102* (50), 10208–10215.

(69) Nelson, J.; Haque, S. A.; Klug, D. R.; Durrant, J. R. Trap-Limited Recombination in Dye-Sensitized Nanocrystalline Metal Oxide Electrodes. *Phys. Rev. V* **2001**, *63* (20), 205321.

(70) Haque, S. A.; Tachibana, Y.; Willis, R. L.; Moser, J. E.; Gra, M.; Klug, D. R.; Durrant, J. R. Parameters Influencing Charge Recombination Kinetics in Dye-Sensitized Nanocrystalline Titanium Dioxide Films. *J. Phys. Chem. B* **2000**, *104* (3), 538–547.

(71) Sampaio, R. N.; Dimarco, B. N.; Meyer, G. J. Activation Energies for Electron Transfer from TiO_2 to Oxidized Dyes: A Surface Coverage Dependence Correlated with Lateral Hole Hopping. *ACS Energy Lett.* **2017**, *2* (10), 2402–2407.

(72) Boschloo, G.; Hagfeldt, A. Activation Energy of Electron Transport in Dye-Sensitized TiO_2 Solar Cells. *J. Phys. Chem. B* **2005**, *109* (24), 12093–12098.

(73) Kopidakis, N.; Benkstein, K. D.; Van De Lagemaat, J.; Frank, A. J.; Yuan, Q.; Schiff, E. A. Temperature Dependence of the Electron Diffusion Coefficient in Electrolyte-Filled TiO_2 Nanoparticle Films: Evidence against Multiple Trapping in Exponential Conduction-Band Tails. *Phys. Rev. B* **2006**, *73* (4), 045326.

(74) Brigham, E. C.; Meyer, G. J. Ostwald Isolation to Determine the Reaction Order for $TiO_2(e^-)|S^+ \leftrightarrow TiO_2|S$ Charge Recombination at Sensitized TiO_2 Interfaces. *J. Phys. Chem. C* **2014**, *118*, 7886–7893.

(75) Tsuda, N.; Nasu, K.; Fujimori, A.; Siratori, K. *Electronic Conduction in Oxides* , 2nd ed.; Cardona, M., Fulde, P., von Klitzing, K., Queisser, H.-J., Merlin, R., Stormer, H., Eds.; Springer: New York, 2000.